

Title	Crustal structure of southern Burkina Faso inferred from magnetotelluric, gravity and magnetic data
Creators	Le Pape, F. and Jones, A.G. and Jessell, M.W. and Perrouty, S. and Gallardo, L.A. and Baratoux, L. and Hogg, C. and Siebenaller, L. and Touré, A. and Ouyi, P. and Boren, G.
Date	2017
Citation	Le Pape, F. and Jones, A.G. and Jessell, M.W. and Perrouty, S. and Gallardo, L.A. and Baratoux, L. and Hogg, C. and Siebenaller, L. and Touré, A. and Ouyi, P. and Boren, G. (2017) Crustal structure of southern Burkina Faso inferred from magnetotelluric, gravity and magnetic data. <i>Precambrian Research</i> , 300. pp. 261-272. ISSN 0301-9268 (Accepted Version)
URL	https://dair.dias.ie/id/eprint/1118/
DOI	http://dx.doi.org/10.1016/j.precamres.2017.08.013

1 **Crustal structure of southern Burkina Faso inferred from**
2 **magnetotelluric, gravity and magnetic data**

3
4 F. Le Pape^a, A. G. Jones^{a,j}, M. W. Jessell^{b,c}, S. Perrouty^c, L. A. Gallardo^d, L. Baratoux^{e,f}, C.
5 Hogg^a, L. Siebenaller^c, A. Touré^g, P. Ouyi^h and G. Borenⁱ

6
7 ^aDublin Institute for Advanced Studies, Ireland

8 ^bCentre for Exploration Targeting, The University of Western Australia, Australia

9 ^cWestern University, Earth Sciences, London, ON, Canada

10 ^dEarth Science Division, Centro de Investigación Científica y de Educación Superior de Ensenada, B.C. México

11 ^eUniversité de Toulouse, CNRS, Géosciences Environnement Toulouse, Institut de Recherche pour le
12 Développement, Observatoire Midi-Pyrénées, 14 Av. Edouard Belin, F-31400 Toulouse, France

13 ^fIFAN Cheikh Anta Diop, Dakar, Senegal

14 ^gBUMIGEB, Burkina Faso

15 ^hUniversity of Ouagadougou, Burkina Faso

16 ⁱUniversity of Adelaide, Australia

17 ^jNow at: Complete MT Solutions, Canada

18

19 **Abstract**

20 Understanding the architecture of the West African craton at depth is essential to be able to
21 reconstruct its evolution. Here, this study focuses on the crustal imaging of structures and
22 geometries characterizing the crust of the Leo-Man shield with broadband and long period
23 magnetotelluric data collected in southern Burkina Faso and covering a 220km long profile. The
24 resulting 3D resistivity crustal model highlights the distribution of the granite-greenstone

25 assemblages with depth showing very good correlation with mapped surficial lithologies. The
26 whole crust of southern Burkina is resistive, with lateral as opposed to vertical major resistivity
27 contrasts, reflecting the location of major-scale shear zones characterizing this part of the
28 Baoulé-Mossi domain. Ground gravity data acquired along the same line as the MT data were
29 also modeled and show relatively good correspondence with the resistivity model. The new
30 resistivity and gravity models compared with results from joint inversion of gravity and
31 aeromagnetic data highlight significant changes between the greenstone belts and granitoid
32 domains along the profile. The comparison of the geophysics with the geology enables us to
33 define new depth constraints of the main tectonic features in the area. The observed large scale
34 dipping shear zones favour the model of crustal building through major parallel thrust faults.

35

36 Keywords: West African craton, Burkina Faso, magnetotellurics, gravity, magnetization, joint
37 inversion

38

39 **1. Introduction**

40 The Leo-Man Shield hosts the Paleoproterozoic lithologies that bound the main Archean
41 nucleus of the southeastern part of the West African craton. The Baoulé-Mossi domain forms the
42 eastern and northern parts of the Leo-Man Craton (Bessoles, 1977) and reflects typical Archean-
43 like greenstone-granitoid assemblages consisting of Birimian volcano-sedimentary belts
44 separated by extensive tonalite-trondjemite-granodiorite and granitoid provinces (Baratoux et
45 al., 2011). Two distinct tectonic models have explained the tectonic evolution of the granite-
46 greenstone domains. The first model invokes a plate tectonics scenario where crustal building

47 involves major parallel thrust faults (Hirdes et al., 1996; Feybesse et al., 2006; Baratoux et al.,
48 2011). In contrast, the second model explains the granite-greenstone formations as a result of
49 vertical motion or sagduction related to gravitational instabilities (Pons et al., 1995; Vidal et al.,
50 2009; Lompo, 2010). Due to a thick lateritic cover, the Paleoproterozoic rocks of the Baoulé-
51 Mossi domain are poorly exposed (Lompo, 2010; Metelka et al., 2011). The use of geophysical
52 techniques to resolve shallow and deeper structures is essential for a better understanding of the
53 structural configuration of the domain at depth.

54 The magnetotelluric (MT) method has proven itself very useful in imaging the lithospheric
55 structures and geometries of various Archean and Proterozoic domains. Major tectonic features
56 are often revealed through compositional variation and deformation in rocks, as expressed
57 through their electrical conductivity, and particularly the presence of conductive graphite,
58 sulfides or saline fluids, whose resolved geometry can help understand the tectonic evolution of
59 suture zones (e.g., Jones et al., 2001; Selway et al., 2009; Miensoopust et al., 2011; Khoza et al.,
60 2013). Although lithospheric-scale regional geophysical studies, and particularly MT, have not
61 been routinely undertaken in West Africa, Ritz (1983, 1984) highlighted the extension of several
62 major tectonic discontinuities deeper in the crust and lithosphere, based on the resistivity
63 modeling of magnetotelluric profiles from northern Burkina Faso, southern Niger and Senegal.
64 More recently Jessell et al. (2016) compiled the existing regional- and global-scale geophysical
65 datasets to help provide a craton -scale framework for future studies.

66 In this study, we aim to provide further depth constraints on the main granite-greenstone
67 assemblages of south-western Burkina Faso described by Baratoux et al. (2011) and Metelka et
68 al. (2011). As part of the West African Exploration Initiative (WAXI) project, broadband and
69 long period magnetotelluric data have been collected along a profile crossing the major

70 lithological units of southern Burkina Faso. The MT data were modeled, using an objective
71 inversion approach, to generate a three-dimensional 3D resistivity model of the crust of Burkina
72 Faso. A new density model was also obtained from forward modeling of ground gravity data
73 acquired along the same transect as the MT data. In order to investigate the evolution at depth of
74 the geophysical properties characterizing the different lithological units observed at the surface,
75 the 3D resistivity model, as well as new gravity model, are discussed and compared with the
76 gravity/geology forward model from Baratoux et al. (2011), and previously unpublished density
77 and magnetization models of the area based on the joint inversion algorithm of Gallardo (2007).

78

79 **2. Geological background**

80 The Baoulé-Mossi domain formed in the Paleoproterozoic between 2250 and 1980 Ma and
81 was subjected to several deformation phases associated with the Eburnean orogeny (Bonhomme,
82 1962; Feybesse et al., 2006; Baratoux et al., 2011). Further north and west, the Paleoproterozoic
83 basement is overlain by the Mesoproterozoic to Paleozoic Taoudeni basin (Fig. 1) (Bronner et
84 al., 1980; Teal & Kah, 2005; Rooney et al., 2010).

85 The greenstone belts of south-western Burkina Faso, extending into northern Ivory Coast and
86 Ghana, show mafic tholeiitic compositions related to oceanic plateaus (Abouchami et al., 1990)
87 and intermediate to felsic calc-alkaline compositions typical of volcanic arc environments
88 (Béziat et al., 2000). The Birimian volcanic rocks characterizing the greenstone belts are overlain
89 by flysch-type sedimentary basins (Baratoux et al., 2011). The Tarkwaian-type sediments, which
90 were deposited after 2120 Ma, have been established as the youngest sequence in the greenstone
91 belts of the Baoulé-Mossi domain (Leube et al., 1990; Bossière et al., 1996; Castaing et al., 2003;

92 Feybesse et al., 2006; Baratoux et al., 2011). The peak of the Birimian volcanism has been dated
93 around 2190-2160 Ma (Davis et al., 1994; Lüdtke et al., 1999; Loh and Hirdes, 1996) whereas
94 Birimian sedimentary basins were dated as young as 2130 Ma (Lüdtke et al., 1999) and 2107 Ma
95 (Doumbia et al., 1998). Therefore, whereas Leube et al. (1990) proposed the volcanic sequences
96 and sedimentary basins to be contemporaneous, some of the sedimentary basins appear to
97 postdate the principal volcanic activity (Agyei Duodu et al., 2009; Baratoux et al., 2011).

98 Western Burkina Faso is characterized by three N-S trending greenstone belts (Fig. 1),
99 defined from west to east as the Banfora, Houndé and Boromo belts (Castaing et al., 2003). Each
100 of them exhibits a similar stratigraphic sequence consisting of basalts and andesites at the base
101 and evolving into volcano-sediments towards the top (Baratoux et al., 2011). The Banfora belt is
102 separated into two parts by the Greenville-Ferkessedougou-Bobo-Dioulasso shear zone (GFBSZ)
103 (Fig. 1) associated with synkinematic granitic intrusions (Lemoine, 1990). East of the GFBSZ,
104 the Banfora belt is composed of basalts, andesites, volcano-sediments and rhyolites, whereas the
105 west of the GFBSZ exhibits volcano-sedimentary sequences only (Baratoux et al., 2011). The
106 Houndé belt shows intermediate to acid calc-alkaline volcanic series in its western part along the
107 Ouango-Fitini shear zone (Fig. 1). To the east, the Boni shear zone characterizes the contact
108 between tholeiitic basalts and gabbro, and Tarkwaian-type sediments. The Tarkwaian-type
109 sedimentary unit represents a 400-km-long corridor stretching down into the Ivory Coast (Fig. 1)
110 (Bossière et al., 1996). The eastern and western parts of the Boromo belt are characterized by a
111 thick sequence of basalts intercalated with gabbros, including also more intermediate and
112 ultramafic units in its eastern part. As it continues into Ghana, the Boromo belt becomes the Wa-
113 Lawra belt (Leube et al., 1990; Duodu et al., 2009, Block et al., 2015). All rocks in this region
114 have been metamorphosed to at least greenschist facies (Baratoux et al., 2011).

115 The granitoid domains separating the different greenstone belts have been named from west
116 to east as the Niangoloko, Sidéradougou and Diébougou domains (Fig. 1). In addition to the
117 well-defined granitoid domains, plutons have also intruded the greenstone belts as relatively
118 small individual granite bodies (Baratoux et al., 2011; Metelka et al., 2011). There is evidence
119 for only a few magmatic episodes contemporaneous with the Birimian volcanism since most of
120 the plutonic activity occurred at a later stage through several magmatic pulses dating between
121 2180 and ~2097 Ma (Hirdes et al., 1996; Doumbia et al., 1998; Castaing et al., 2003; Duodu et
122 al., 2009).

123

124 **3. Magnetotelluric soundings**

125 3.1 Data acquisition and processing

126 Magnetotelluric impedances, which contain information about the lateral and vertical
127 variation in electrical conductivity of the subsurface, are obtained from recording the Earth's
128 natural electromagnetic (EM) variations with time. In the frequency domain, the MT transfer
129 function Z or MT impedance tensor describes the direct linear relationship between the measured
130 horizontal components of the electric (E_x , E_y) and magnetic (H_x , H_y) fields (Chave and Jones,
131 2012).

132 As part of the West African Exploration Initiative (WAXI) project, MT data were collected
133 in south-west Burkina Faso between February and March 2013 using broadband Phoenix
134 Geophysics (Toronto) MTU5A and long period LEMI-417M (Lviv Centre of Institute for Space
135 Research) instruments with an approximate 10 km spacing between broadband sites, every 30
136 km for the long period stations. The orientation of the profile resulting from the acquisition
137 layout was chosen to cross perpendicularly most of the north-south trending greenstone belts and

138 granitoid domains of southern Burkina Faso (Fig. 1). The MTU5A recorded electric and
139 magnetic time series data were processed using the standard robust processing of the commercial
140 code from Phoenix Geophysics based on Jones and Jödicke (1984), which is based on a Least
141 Trimmed Squares robust technique proposed independently by Rousseeuw (1984). When
142 available, the LEMI-417 long period data (only acquired at sites bur013, bur020, bur023, bur026,
143 bur028 and bur033) were processed after the method of Smirnov (2003). The broadband data
144 were recorded over 3 days whereas the long period stations were left in the ground for around 20
145 days. Some of the broadband data are a bit noisier for periods above 100s and some points had to
146 be removed. When possible the broadband and long period data were merged at common
147 locations for periods between 100 and 1000s, considering the broadband data as the shifting
148 reference. Overall the data are overlapping quite well. Multiple sites were recorded
149 simultaneously, enabling the use of remote referencing methods (Gamble et al., 1979), in order
150 to reduce bias effects and improve the quality of the estimated MT responses. For this study, we
151 limit the periods of investigation from 10^{-2} s to 1000 s, i.e., frequencies of 100 Hz to 0.001 Hz.
152 As the main focus here is the investigation of the crust beneath southern Burkina Faso, it was
153 determined that periods ranging up to 1000 s penetrate sufficiently deep to resolve the whole
154 crust due to the high resistivity of the area. Furthermore, it appeared the effect of the equatorial
155 electrojet (Mareschal, 1986) were negligible for period below 1000s but should be taken into
156 account for more lithospheric scale studies including periods above 1000s. No vertical magnetic
157 component was recorded on broadband stations. For the long period stations, induction vectors
158 were considered but they are strongly affected by the equatorial electrojet. It is the case for even
159 shorter periods than 1000s compared to the effects of the electrojet on the impedance tensor
160 mainly appearing for periods higher than 1000s as mentioned above.

161

162 3.2 Data, Phase tensor and Dimensionality analysis

163 Data quality is generally good at most stations. Figure 2a and Figure 4 show the four
164 components of a some selected sites across the profile. A lot of sites exhibit phases out-of-
165 quadrant which is a clear evidence of 3D response. High apparent resistivity values can also be
166 seen in all components for several stations highlighting the complexity of the study area and
167 justifying the use of full tensor inversion. For instance, the responses of the MT tensor diagonal
168 elements XX and YY cannot be neglected even when rotating the data in any particular strike
169 direction. Moreover, due to the complexity of the tectonic setting, sites show different levels of
170 distortion such as static shifts. For example, the significant split in the apparent resistivity curves
171 at high frequency for site bur021 (Fig. 2a) may be associated with static shift. However, the
172 static shift problem can be very tricky as at a single site not all curves may necessarily be
173 affected and sometimes just one or two can be shifted up or down. It is worth mentioning also
174 that site bur024 and bur031 were not considered for this study since the responses were highly
175 distorted, which explains the gaps observed in the MT profile (Fig. 1). As discussed later those
176 stations were still included in the early stage of the modeling but discarded on the final results.

177

178 The MT phase tensor (Caldwell et al., 2004) represented as an ellipse is a really useful tool to
179 obtain qualitative information about the dimensionality and distribution of the regional
180 conductivity structures in a 3D environment. In isotropic 2D cases, the ellipse axes are parallel
181 and perpendicular to the 2D strike direction. However, in 3D cases, the coordinate-invariant
182 skew angle β defines the deviation of the phase tensor principal axes from an equivalent
183 symmetric configuration resulting from the asymmetry of the phase responses produced by 3D

184 structures (Heise et al., 2006). Figure 2b highlights the phase tensor skew values at each site for
185 different periods (depth) which also reveals the complexity of the data over the whole profile. It
186 is however important to keep in mind that due to the non-representation of error of the ellipses
187 plots, one must be careful when interpreting the phase tensor plots. The skew angles show a
188 significant number of frequencies and sites with values outside the $[-5^\circ \ 5^\circ]$ interval and therefore
189 exceeding the limits of 2D approximations. Overall, long periods exhibit relatively high skew
190 values. However, for shorter periods, the ellipses define a mix between 2D and 3D-like clusters
191 across the profile which appear to be consistent with lithological units (Fig. 1). The granitoid
192 domains ellipses are defined by low β values and show consistent orientations between several
193 neighbour sites. For sites located on or at proximity of the greenstone belts, ellipses show high β
194 values and more abrupt changes in orientations between neighbour sites. Furthermore, flattened
195 ellipses observed at very short periods ($< 0.1s$) for sites bur016 and bur023 can be explained by
196 the presence of very high conductivity contrasts related to the major shear zones (Fig. 1). The
197 ellipses orientations show a good agreement with the north-south trend of the greenstone belts
198 and shear zones characteristic of the study area (Fig. 1). However, although the data shows some
199 2D-like behaviour for clustered sites and periods, the 3D signature is too broad and significant to
200 be neglected.

201

202 **4. 3D resistivity modeling**

203 Despite the “single-profile” layout of the stations, which is not optimal for 3D
204 modeling/inversion, the significant 3D signatures of the responses for a broad range of MT
205 stations requires the use of 3D approaches. Having only MT data collected along a single profile,

206 2D modeling of the data should come to mind, however the 2D modeling of 3D data would bring
207 significant artefacts in the final models inhibiting interpretations (Ledo et al., 2002).

208

209 4.1 3D full tensor inversion

210 Two 3D inversion codes WSINV3DMT (Siripunvaraporn et al., 2005) and ModEM
211 (Egbert and Kelbert, 2012) as well as different inversion steps were considered through the
212 inversion process. At the end, mainly the code ModEM was used for models testing and to
213 compute the final 3D models due to a faster convergence of the code to an acceptable misfit.
214 However, it is worth noting that results from both inversion algorithms revealed similar
215 structures, including conductors, which is also comforting the robustness of the inversion results
216 presented here. The data were inverted simultaneously for all 4 impedance tensor elements and
217 an error floor of 5% was used to set a minimum error bar of $0.05 * \sqrt{Z_{xx}Z_{yy}}$ on the diagonal
218 and $0.05 * \sqrt{Z_{xy}Z_{yx}}$ on the off-diagonal elements of the impedance tensor during the
219 inversion. Although different starting models have been tested, the starting (and a priori) model
220 used for the initial inversion was a 150 km thick layer of 500 Ω .m with resistivity decreasing
221 gradually from 150 km to 410 km where a fixed 10 Ω .m halfspace was locked during inversion.
222 The later represents the mantle transition zone and is necessary in 2D and 3D modeling to
223 prevent bleeding down of features and satisfy the boundary condition on the base of the model.
224 The 3D mesh used for the inversions is defined as 81 x 152 x 51 cells with a 2 x 2 km horizontal
225 gridding at the vicinity of the stations. Periods ranging from 10^{-2} s to 1000 s were modeled for
226 crustal structures, which were assumed to extend to the average Moho depth of 30 km beneath
227 the profile (Pasyanos and Nyblade, 2007). 3D inversions were performed in several steps where
228 different schemes and station combinations have been tested. As mentioned previously, stations

229 bur024 and bur031 are not considered in the final results due to some highly distorted responses
230 characterized by higher misfits in the inversions. Removing those stations however did not affect
231 significantly the structures of the models, for example by adding or removing conductive
232 anomalies. Furthermore, two particular schemes were investigated in the inversion steps.
233 Inversions have been performed by modeling higher frequency first and introducing
234 progressively the lower frequencies but also by modeling longer periods first and introducing
235 progressively the higher frequencies. Both schemes lead to similar structures. For this data set,
236 inverting the high frequency first introduced shallow structures “locked” through the different
237 iterations and therefore affecting the data fit for some stations at longer periods. However,
238 inverting for long period first helped improve the fitting of the long period data as well as the
239 higher frequency data associated with shallower structures. Finally, the effects of some sites have
240 been tested but as discussed below the main differences were observed for the least constrained
241 sites located at the extremities of the profile.

242

243 4.2 model A vs model B

244 The two best models obtained from ModEM and highlighting consistent structures
245 through the different inversion tests, including conductors C1, C2 and C3, are discussed in
246 Figure 3. Whereas model B was obtained after inverting all 22 sites (Fig. 3c), the preferred
247 model A (Fig. 3b) did not include site bur010 in the inversion. Both models are very similar but,
248 as shown by Figure 3d, they differ in the location of the conductive anomaly observed on the
249 western end of the profile (below station bur010). Whereas model B places the anomaly in the
250 middle and lower crust beneath the profile, model A places the anomaly north of the profile in
251 the upper crust. This anomaly is likely real as it is seen by more than one station, however being

252 located at the edge of the profile, its location becomes poorly constrained by the lack of data
253 coverage. The comparison of models A and B shows that interpretation of 3D inversion of a
254 single profile must be taken with care. The lack of constraints on anomalies derived from 3D
255 inversions of single profiles have been discussed in Kiyani et al. (2013) and Wei et al. (2014).
256 Despite being seen by the data, the locations of certain anomalies are not so well constrained
257 particularly at the edges of the profile. Further tests have also been carried out by removing other
258 stations to see their influence on the final models but most observed features remained quite
259 robust. Furthermore, whereas model A shows an overall Root Mean Square (RMS) misfit of 2.7,
260 model B is defined by an RMS of 2.95. The difference in RMS between model A and B is
261 mainly reflecting a better fit of the data (not only for western sites) due to the absence of a lower
262 crustal conductor right below the profile brought by station bur010. Therefore model A was
263 chosen as the preferred model for the area. Despite being associated with a better fit to the
264 overall data, the conductive anomaly observed on model A off-profile (north-west of horizontal
265 slices Fig. 3b) is still not very well constrained and will not be discussed further in this paper.

266

267 4.3 Final 3D resistivity model A

268 The observed and predicted apparent resistivities and phases from model A are compared
269 on Figure 4. The responses derived from the impedance tensor are shown for all 4 components of
270 the tensor and are plotted as apparent resistivity and phases. Overall, the observed and modeled
271 data are very similar, showing only some localized exceptions. The comparison of observed and
272 predicted curves show that the 3D characteristic of the data such as phases out-of-quadrant as
273 well as XX and YY component are relatively well fitted. For example, the observed and
274 predicted responses for site bur025, close to conductor C2, reveal higher misfits at high

275 frequencies but overall the data is quite well recovered. Despite having some of the worst misfits
276 localized at shorter periods for a few stations, Figure 4 shows that the data fit between observed
277 and modeled responses remains quite good at shorter periods for all four components of the
278 tensor. This observation can be mainly accounted for the use of a fine grid (2 x 2 km) at
279 proximity of the stations which significantly improved the resolution on 3D effects for shorted
280 periods and particularly for XX and YY components. The use of a finer mesh would eventually
281 improve the modeling of shorter periods but was limited by computation resources.

282 The 2D cross-section derived from the 3D model A and presented on Figure 3a defines a
283 good representation of the most robust resistive and conductive features characterizing the crust
284 of southern Burkina Faso. Generally, the main features in the data that can be seen on the
285 responses (Fig. 2 and 4) are quite well represented in the resistivity model (Fig. 3a and 3b). The
286 3D model particularly highlights the juxtaposition between highly resistive (purple) and less
287 resistive (green) areas corresponding to the surficial signature of the granitoid domains as well as
288 granite intrusions and greenstone belts, respectively. Overall, the crust beneath southern Burkina
289 Faso is quite resistive with major lateral changes correlating very well with the observed geology
290 (Fig. 3). It is worth noting that compared to the greenstone belts, the lower crust of the granitoid
291 domains is very resistive which may highlight a difference in composition of the lower crust or
292 difference in past alteration. The Greenville-Ferkessedougou-Bobo Dioulasso Shear Zone
293 (GFBSZ), Ouango-Fitini Shear Zone (OFSZ) and Boni Shear Zone (Boni SZ) are defined by
294 large resistive contrasts that extend to the lower crust. On the other hand, the West Batié Shear
295 Zone (WBSZ) which divides two highly resistive blocks of the Diébougou Granitoid Domain
296 (DGD) does not seem to extend further than the middle crust. The Sidéradougou Granitoid
297 Domain (SGD) is divided into two parts: a highly resistive eastern bloc extending probably

298 further into the mantle and a western part more heterogeneous, alternating resistive and more
299 conductive features, which might be linked to the GFBSZ at depth. Finally, three significant
300 conductive anomalies located in the upper crust can be observed on the resistivity model. From
301 west to east, they are defined as conductors C1, C2 and C3 (Fig. 3a and 3b). Conductive anomaly
302 C1 is very localized and is found in the first 5 km of the SGD crust. The anomaly C2 is the most
303 significant in terms of depth and width and is associated with the Houndé belt. Finally,
304 conductive anomaly C3 is located right on the WBSZ.

305 **5. Gravity data and modeling**

306 Ground gravity data were acquired along the same profile as the MT data, with an average
307 spacing of 2 km between each recording points. The ground gravity data were measured using a
308 gravimeter Scintrex CG-3. This device registered 120 measurements at each location and an
309 average value was provided. Data processing includes tide correction, instrumental drift
310 correction (some points were measured multiple times) and latitude correction (calculated using
311 1967's formula of Sheriff, 1984). A differential Ashtech GPS system was used for accurate
312 positioning. The Bouguer anomaly was derived using a density value of 2.67 g/cm^3 taking into
313 account SRTM topography within a radius of 40 km around each recording site. A low-pass filter
314 corresponding to wavelengths above 10 km was applied on the Bouguer anomaly in order to
315 focus the modeling on large-scale density contrasts for better comparison with the resistivity
316 model. It is also worth mentioning that the regional Bouguer anomaly associated with a low-pass
317 filter above 200 km revealed an overall anomaly decreasing from west to east, which could
318 reflect variations of density at depth and particularly lateral changes in the Moho. However,
319 according to Pasyanos and Nyblade (2007) if any change in the Moho occurs at depth beneath
320 the profile, it would likely correspond to a reduction of the crustal thickness towards the eastern

321 end of the profile, which would generate an opposite trend in the evolution of the gravity
322 anomaly along the profile (low to high anomaly from west to east). As a consequence, the
323 regional Bouguer anomaly for wavelengths above 200 km was kept for modeling of the data,
324 assuming the overall variations were more likely related to shallower structures. Observed
325 gravity anomalies can be explained by a variety of mass distributions at different depths. The
326 forward modeling of the gravity data was performed using the gravity tools implemented within
327 the WinGLink package of formerly Geosystem, now Schlumberger. The density model (Fig. 5b)
328 was obtained from forward modeling of the Bouguer anomaly data (Fig. 5a) taking into account
329 the resistivity contrasts observed on the 3D resistivity model as well as surficial geology and
330 gravity models from Baratoux et al. (2011).

331 For consistency with the density values described in Metelka et al. (2011) and Baratoux
332 et al. (2011), similar densities were considered for the different sequences. However, since a
333 low-pass filter was applied on the Bouguer anomaly, the modeled density values represent more
334 of an average density, or deviations from a reference value, rather than absolute density values.
335 A reference density of 2.75 g/cm^3 was chosen for most of the crust based on density values for
336 granitoid domains (Baratoux et al. 2011). Granitic intrusions were assumed a density of 2.7
337 g/cm^3 except for the pluton intrusions at the proximity of the Boromo belt for which densities
338 were assumed as low as 2.65 g/cm^3 . The greenstone belts were modeled with densities of 2.8 ,
339 2.85 and 2.9 g/cm^3 reflecting differences in the volcanic lithologies observed at the surface. A
340 density of 2.95 g/cm^3 for the more mafic to ultramafic rocks exposed west of the Boromo belt
341 corresponds to significant gravity highs. Although less extensive around the recording area, the
342 eastern part of the Banfora belt, in the vicinity of the GFBSZ, is characterized by the presence of
343 more widespread basalts and andesites further south of the profile. Since they are not apparent at

344 the surface along the profile, those units were modeled at depth with higher density values in
345 order to explain the observed gravity high. Similarly, the mafic rocks associated with the OFSZ
346 were also modeled with higher densities (Fig. 5b). Furthermore, it is worth noting that the
347 Banfora greenstone belt appears to be thicker than the Houndé belt, assuming both belts have
348 more or less the same composition, i.e., the same densities of the same lithologies. In order to
349 obtain relatively similar thickness of high density material for the Houndé belt, the volume or
350 size of less dense granitic material would have to be increased.

351 Resistivity and density do not have a straightforward relationship but they can still be
352 compared qualitatively, particularly in this study where greenstone belts associated with denser
353 material appear as more conductive features, particularly the Houndé belt and the granitoid
354 domains related to less dense material reflect very high resistivities (Fig. 5c). Such relationships
355 bring some further constraints on the evolution of the different tectonic features with depth.
356 Conductivity gradients revealed by the phase tensor data (Fig. 2) can also be correlated with the
357 steeper gravity gradients from the Bouguer anomaly data (Fig. 5a) observed close to the main
358 shear zones. There are several density features that correlate fairly well with the resistivity cross-
359 section (Fig. 5c). One feature that particularly seems to be very well constrained by the
360 resistivity model is the large granitic body (Gaoua batholith) located east of the WBSZ between
361 mafic lithologies. Furthermore, the less dense volcanic lithologies of the Houndé belt correlate
362 very nicely in depth and width with the highly conductive anomaly C2 (Fig. 3). Finally, the fact
363 that based on the gravity model, the Banfora greenstone belt is extending in further at depth west
364 of the GFBSZ, help explaining the differences in resistivity between the western and eastern part
365 of the SGD. It is important to keep in mind that a more complex gravity model with sharp
366 contrasts as seen in the resistivity model could probably fit the Bouguer anomaly as well.

367 However, the aim here was to present a relatively simple “geological” density model that match
368 with the surficial geology and help understand better the observed resistivity contrasts at depth.

369

370 **6. Discussion**

371 6.1 Electrical resistivity of southern Burkina Faso

372 Overall, apart from the first top 3 km, the main shear zones and conductive anomalies C1, C2
373 and C3 localized in the upper crust, most of the crust is remarkably resistive throughout its whole
374 extent. Although differences in resistivity are fairly clear between greenstones belts and granitoid
375 domains, there is no significantly conducting lower crust, which is usually observed in
376 continental settings (Jones, 1992; Hyndman et al., 1993). Furthermore, conductive lower crust
377 has also been imaged in stable plate interiors, although less expected when compared to
378 Paleozoic regions. Parts of the Kaapvaal and Zimbabwe cratons in south Africa (Muller et al.,
379 2009; Miensopust et al., 2011; Khoza et al., 2013) but also the northeastern Rae craton region in
380 Canada where Evans et al. (2005) revealed the presence of a broadly conductive lower crust (50
381 Ωm). The enhanced conductivity of the lower crust pervasively observed in Proterozoic and
382 younger terranes has been explained by the presence of saline fluids (Jones, 1987, 1992;
383 Hyndman et al., 1993; Wannamaker, 2000), although they may not be stable at those depth
384 (Yardley and Valley, 1997). Graphite films along grain boundaries have also been proposed to be
385 good candidates (Hyndman et al., 1993), although mechanical deformation could affect graphite
386 connectivity in the lower crust (Glover, 1996) and recent laboratory experiments would appear to
387 exclude this hypothesis (Yoshino and Noritake, 2011). The highly resistive lower crust of south-
388 western Burkina Faso is more likely defined by the presence of dry granulite rocks characterized
389 by a lack of extensive interconnected graphite films. Spratt et al. (2009) also imaged a resistive

390 lower crust beneath the Proterozoic Wopmay orogen abutting the Slave Craton. Finally, it is
391 worth noting that Ritz (1983) also highlighted the presence of a resistive lower crust in northern
392 Burkina Faso, consistent with our results.

393 The upper crust however shows larger conductivity contrasts and reveals the presence of
394 three striking conductive anomalies ($< 50 \Omega.m$). The relatively low resistivity of the greenstone
395 belts and particularly the Houndé belt can be explained by the presence of the volcano-sediments
396 in the upper crust but also by the broad number of faults, in contrast to the granitoid domains
397 (Fig. 1). The fault and shear zones present within or at the boundary of the greenstone belts
398 create pathways for fluids, increasing the overall bulk conductivity. Those fluids could also have
399 precipitated into more conductive phases such as graphite or sulphides. Křibek et al., 2008
400 discussed on the presence of graphite in sub-greenschist and greenschist facies of the Kaya-
401 Goren greenstone belt, an extension of the Houndé belt in northern Burkina Faso. In the case of
402 the Houndé belt, the conductivity anomaly C2 matches very well with the volcano-sediments
403 belonging to the Lower Birimian sequence (Feybess and Milesi, 1994; Křibek et al. 2008) and
404 could therefore be as well explained by the presence of graphite in the sequence. To the east, the
405 conductive anomaly C3 characterizing the WBSZ is also significant. It is worth mentioning the
406 presence further north of the Perkoa massive volcanogenic sulphide deposit hosted by the Lower
407 Birimian sequences of the Boromo Belt (Schwartz and Melcher, 2003). Therefore other sulphide-
408 rich intrusion may have happened further south on the western flanks of the Boromo belt. The
409 anomaly however could also be linked to the presence of fluids or crystallized graphite along the
410 shear zone. Finally, the last significant conductive anomaly C1 observed on the profile and
411 located in the middle of the Sidéradougou domain does not seem to match with any particular

412 fault or shear zones, the Bossié shear zone (Baratoux et al. 2011) being located more to the east.
413 However, it correlates quite well with a high magnetic contrast which is discussed below.

414 6.2 Crustal structure interpretation

415 The cross-gradient inversion scheme of Gallardo (2007) has been applied to gravity
416 (NGA/BGI) and magnetic (BUMIGEB aeromagnetic survey derived grids) datasets for Burkina
417 Faso. The cross-gradient inversion technique mainly focuses on the structural similarity between
418 the distribution of different geophysical properties, reducing the non-uniqueness of the inversion
419 process for each data type. While the density and magnetization models across southern Burkina
420 Faso derived from cross-gradient inversion can be used for a correlative interpretation, we prefer
421 to use the associated red-green geospectral image representation as used in Gallardo and
422 Thebaud (2012) and Gessner et al. (2016). This image bears the integrated structure-
423 multiproperty value representation and is presented on Figure 6 in comparison with the new
424 (inverse) resistivity and (forward) gravity models, as well as the gravity-geology forward model
425 from Baratoux et al. (2011) matching in location with the eastern part of the MT profile. The
426 density variations observed in Figure 6d from Gallardo's inversion are in reasonably good
427 agreement with the gravity models presented in Figures 6a and 6b from forward modeling,
428 exhibiting low and high density values for granitoid domains and greenstone belts, respectively.
429 The resemblance to the MT section is more outstanding, showing a high correlation of the most
430 electrical conductors (labelled A to E on Fig. 6c and 6d) to deeper high
431 magnetization/intermediate density features. It also shows a match of the major resistors to
432 shallower greenstone and intrusive terrains identifiable in the geospectral image (e.g. feature
433 labelled 1 on Fig. 6c and 6d). The variations of magnetization along the profile highlight
434 relatively high magnetic contrasts at depth beneath the more mafic sequences associated with

435 each greenstone belt. Variations in rock bulk susceptibility reflect mainly variations in magnetite
436 content (Metelka et al., 2011). Compared to gravity, magnetic anomalies are more difficult to
437 interpret since high magnetic mineral phases equally occur in granites and mafic rocks.
438 However, it is worth noting that, in Burkina Faso, basalts and gabbros have been associated with
439 high susceptibility anomalies and volcanic sediments with low anomalies, whereas granitoids
440 reflect both low and high magnetization (Metelka et al., 2011). The Niangoloko granitoid domain
441 (Fig. 1) does not seem to show a significant signature either on the resistivity or the gravity
442 models (Fig. 6) and it is undistinguishable from the Banfora belt signature in the geospectral
443 image. According to all these evidences, it seems reasonable to expect that the Banfora belt may
444 also expand further west at depth compared to its surficial trace (Fig. 7). Furthermore, one main
445 difference between the Banfora belt and both the Houndé and Boromo belts is the observed
446 broad lower magnetic signature of its upper crust (reflected in distinctive green tones in the
447 geospectral image in 6d) compared to the other two belts showing high magnetic anomalies. This
448 low magnetic anomaly of the Banfora belt is also presented in Metelka et al. 2011, indentifying
449 the GFBSZ as a “set of demagnetized” shear zones. On the contrary, both Houndé and Boromo
450 belts reveal highly magnetic mafic and ultramafic intrusions on their flanks that can account for
451 the observed anomalies.

452 The Sidéradougou and Diébougou granitoid domains, the low density structure observed in
453 the geospectral image of Figure 6d shows a clear correlation with the high resistivity of the crust
454 extending across the whole crust. The Houndé belt shows a smaller density imprint than the
455 Banfora belt. Assuming both belts can be modeled by similar density values, the Houndé belt
456 cannot be modeled as thick as the Banfora belt unless intruded by more (low density) plutonic
457 material. In fact, the density variations in Figure 6d illustrate the presence of low densities in the

458 eastern part of the Houndé belt. The OFSZ located west of the Houndé belt is associated with
459 very high density and high magnetic heterogeneities (Figs. 6b and 6d) extending in depth and
460 confirming the observations from the resistivity model that the OFSZ is a significant crustal
461 feature that may be extending further in the mantle. Furthermore, in addition to other shear zones
462 across the profile, the Boni shear zone bounding the east side of the Houndé belt also shows a
463 strong contrast at depth in resistivity. The western part of the Boromo belt delimited by the
464 WBSZ is clearly highlighted by all geophysical techniques, showing significant increases in
465 density, resistivity and susceptibility. However, the geospectral image does not reveal the
466 presence of the Gaoua batholith or the Boni shear zone located west of the Boromo belt,
467 although its signature is quite clear on the new gravity and resistivity models (Fig. 5). This
468 difference is explained by the absence of actual ground gravity data in the regional polygons
469 used for joint inversion for this region. This also prevents the detection of any density-
470 magnetization heterogeneity that may correlate to the marked conductor C3. Concerning the
471 conductive anomalies C1 and C2, the magnetic and density signatures allow us to confirm or
472 improve their interpretations. C1 and C2 have low density but correlates very well with a high
473 magnetic blob, which corroborates with the interpretation of the presence of graphite. Although,
474 as discussed above, C3 might not be properly resolved on the geospectral image (Fig. 6d), the
475 observed lower magnetization associated with the conductive anomaly may be only related to the
476 presence of fluids in the shear zone, instead of highly magnetic graphite or sulfides.

477 6.3 Structural constraints at depth

478 The geophysical models discussed here show clear correlations between each other and
479 particularly bring further constraints at depth on the tectonic structures involved in the area.
480 Overall, the major resistivity contrasts reveal the extension of major shear zones that divide or

481 bound the main greenstone belts. The dipping orientations of the major contacts and shear zones
482 have been plotted in Figure 7. West of the profile, the GFBSZ is defined by west- and east-
483 dipping structures. The geometry of the OFSZ system is in very good agreement with the
484 gravity model from Baratoux et al. (2011) (Fig. 6a) showing two trends: a sub-vertical
485 orientation to the west and a very pronounced eastward dipping structure to the east. Further east,
486 although Baratoux et al. (2011) described the Boni shear zone as an east-dipping structure, the
487 resistivity model reveals that the Boni shear zone might be dipping to the west instead. Moving
488 closer to the Gaoua batholith, the structures including the WBSZ appear more sub-vertical.
489 Those trends in the crustal scale resistivity contrasts are also seen and confirmed on the different
490 vertical cross-sections of the 3D resistivity model (Fig. 3b). Furthermore, despite being a single
491 profile, the horizontal slices through the 3D model at different depths (Fig. 3b and Fig. 7)
492 highlight the preferred north-south orientated extent of the major shear zones as deep as the
493 Moho. In fact, the lateral variations observed on the global Bouguer anomaly map compares
494 quite well with the lateral distribution of the resistivity contrasts at depth, as well as the surficial
495 geology (Fig. 7). Therefore, although the lateral resistivity variations at depth are associated with
496 the modeling of a single profile, they still reveal some consistent and interesting information on
497 the distribution of the main terranes deeper in the crust. The presence of sub-vertical and steeply
498 dipping lateral resistivity contrasts, associated with major thrust faults and shear zones, that
499 divide the whole crust and possibly extend into the mantle (Fig. 7), reflects the very strong
500 shortening that affected the region through time. The observed large-scale signatures of the
501 Greenville-Ferkessedougou-Bobo Dioulasso, Ouango-Fitini Shear Zone, Boni and West Batié
502 shear zones may favour the model of crustal thickening through nappe stacking along parallel
503 thrust faults (Hirdes et al., 1996; Feybesse et al., 2006; Baratoux et al., 2011).

504

505 **7. Conclusion**

506 As expected and clearly highlighted by the MT data, the Leo-man shield is a very difficult area
507 to model and interpret. In such a complex tectonic setting, the modeling and interpretation of
508 MT data can be quite challenging and the need for the integration of several geophysical
509 techniques and data sets becomes significant. For instance, not only the multi- geophysical
510 approach including density and magnetization contrasts defines a more robust interpretation of
511 the main crustal features but it also comforts on the validity of the main features revealed by
512 the 3D resistivity model. Overall, the results enable to differentiate and highlight the structure
513 of the granite-greenstone formations of the Baoulé-Mossi domain at depth, but also reveal the
514 extent of significant shear zones likely extending further in the mantle.

515

516 **Acknowledgments**

517 A big thank you to the SOS Sahel crew for their tremendous contribution in the planning
518 and execution of the MT fieldwork but also for facilitating the communication with local
519 villages. Special thanks the IRD centre in Ouagadougou and particularly Moumouni Koné and
520 Frédéric Cazenave for their help and support during MT fieldwork preparation. We also would
521 like to thank Sylvain Bonvalot for helping out with the gravimeter and Saga Sawadogo from the
522 University of Ouagadougou for the logistics on the gravity fieldwork. This work was funded by
523 the West African Exploration Initiative (WAXI), and we wish to gratefully acknowledge
524 AMIRA International and the industry sponsors. Thank you also to Maxim Smirnov for
525 providing his processing code, Weerachai Siripunvaraporn for providing the 3D inversion code
526 WSINV3DMT and Gary Egbert for providing the 3D inversion code ModEM. We would like to

527 thank the Irish Centre for High Performance Computing (ICHEC) for availing the FIONN cluster
528 to carry out the numerical computations and Jan Vozar, Hao Dong and Gaofeng Ye for providing
529 matlab visualisation tools for 3D MT results. Finally, special thanks to the local villagers for
530 their help and welcoming during the installations of the magnetotelluric stations.

531

532 **References**

533 Abouchami, W., Boher, M., Michard, A., Albarède, F., 1990. A major 2.1 Ga event of mafic
534 magmatism in West Africa; an early stage of crustal accretion. *Journal of Geophysical Research,*
535 *B, Solid Earth and Planets* 95 (17) (629), 605-617.

536 Agyei Duodu, J., Loh, G.K., Hirdes, W., Boamah, K.O., Baba, M., Anokwa, Y.M., Asare, C.,
537 Brakohiapa, E., Mensah, R.B., Okla, R., Toloczyki, M., Davis, D.W., Glück, S., 2009.

538 *Geological Map of Ghana 1:1,000,000.* BGS/GGS, Accra, Ghana/Hannover, Germany.

539 Balmino, G., N. Vales, S. Bonvalot, and A. Briais, 2012. Spherical harmonic modelling to ultra-
540 high degree of Bouguer and isostatic anomalies. *Journal of Geodesy* 86, 499-520.

541 Baratoux, L., Metelka, V., Naba, S., Jessell, M. W., Gregoire, M., Ganne, J., 2011. Juvenile
542 paleoproterozoic crust evolution during the eburnean orogeny (2.22.0 ga), western burkina faso.
543 *Precambrian Research* 191, 18-45.

544 Bessoles, B., 1977. *Géologie de l'Afrique. Le craton Ouest-Africain mémoires.* BRGM, Paris,
545 88.

546 Béziat, D., Bourges, F., Debat, P., Lompo, M., Martin, F., Tollon, F., 2000. A Paleoproterozoic
547 ultramafic-mafic assemblage and associated volcanic rocks of the Boromo greenstone belt:
548 fractionates originating from island-arc volcanic activity in the West African craton. *Precambrian*
549 *Research* 101, 25-47.

550 Block, S., Ganne, J., Baratoux, L., Zeh, A., Parra-Avila, A. L., Jessell, M., Ailleres, L.,
551 Siebenaller, L., 2015. Petrological and geochronological constraints on lower crust exhumation
552 during Paleoproterozoic (Eburnean) orogeny, NW Ghana, West African craton. *Journal of*
553 *Metamorphic Geology* 33, 463-494.

554 Bonhomme, M., 1962. Contribution à l'étude géochronologique de la plate-forme de l'Ouest
555 Africain. *Annals de la Faculté des Sciences de Université de Clermont-Ferrand Géol. Minéral* 5
556 (62).

557 Bossière, G., Bonkougou, I., Peucat, J.-J., Pupin, J.-P., 1996. Origin and age of
558 Paleoproterozoic conglomerates and sandstones of the Tarkwaian Group in Burkina Faso, West
559 Africa. *Precambrian Research* 80, 153-172.

560 Bronner, G., Roussel, J., Trompette, R., 1980. Genesis and geodynamic evolution of the
561 Taoudeni cratonic basin (Upper Precambrian and Paleozoic), Western Africa. *Dyn. Plate Int.*
562 *Geodyn. Series* 1, 8190.

563 Caldwell, T. G., H. M. Bibby, Brown, C., 2004. The magnetotelluric phase tensor, *Geophys. J.*
564 *Int.*, 158, 457–469.

565 Castaing, C., Billa, M., Milési, J. P., Thiéblemont, D., Métour, J. L., Egal, E., Donzeau, M.,
566 Guerrot, C., Cocherie, A., Chèvremont, P., Tegye, M., Itard, Y., Zida, B., Ouedraogo, I., Koté,

567 S., Kabore, B. E., Ouedraogo, C., Ki, J. C., Zunino, C., 2003. Notice explicative de la carte
568 géologique et minière du Burkina Faso à 1/1 000 000, 147.

569 Chave, A. D., Jones, A. G., 2012. The Magnetotelluric Method: Theory and Practice. Cambridge
570 University Press, New York.

571 Davis, D. W., Hirdes, W., Schaltegger, U., Nunoo, E. A., 1994. U-Pb age constraints on
572 deposition and provenance of Birimian and gold-bearing Tarkwaian sediments in Ghana, West
573 Africa. *Precambrian Research* 67, 89-107.

574 Doumbia, S., Pouclet, A., Kouamelan, A., Peucat, J. J., Vidal, M., Delor, C., 1998. Petrogenesis
575 of juvenile-type Birimian (Paleoproterozoic) granitoids in Central Cote-d'Ivoire, West Africa:
576 geochemistry and geochronology. *Precambrian Research*. 87, 3363.

577 Duodu, J. A., Loh, G. K., Hirdes, W., Boamah, K. O., Baba, M., Anokwa, Y. M., Asare, C.,
578 Brakohiapa, E., Mensah, R. B., Okla, R., Toloczyki, M., Davis, D. W., Glück, S., 2009.
579 Geological map of Ghana 1:1 000 000. BGS, GGS, Accra (Ghana), Hannover (Germany).

580 Egbert, G., Kelbert, A., 2012. Computational recipes for electromagnetic inverse problems.
581 *Geophysical Journal International* 189, 251–267.

582 Evans, S., Jones, A. G., Spratt, J., Katsube, J., 2005. Central Baffin electromagnetic experiment
583 (CBEX) maps the NACP in the Canadian arctic. *Physics of the Earth and Planetary Interiors* 150,
584 107-122.

585 Feybesse, J.L., Milesi, J.P., 1994. The Archaean/Proterozoic contact zone in West Africa: a
586 mountain belt of decollement thrusting and folding on a continental margin related to 2.1 Ga
587 convergence of Archaean cratons? *Precambrian Research* 69, 199–227.

588 Feybesse, J. L., Billa, M., Guerrot, C., Duguey, E., J.-L., Milési, J.-P., Bouchot, V., 2006. The
589 Paleoproterozoic Ghanaian province: geodynamic model and ore controls, including regional
590 stress modeling. *Precambrian Research* 149, 149-196.

591 Gallardo, L. A., 2007. Multiple cross-gradient joint inversion for geospectral imaging.
592 *Geophysical Research Letters* 34 (L19301).

593 Gallardo, L.A., Thebaud, N., 2012. New insights into Archean granite greenstone architecture
594 through joint gravity and magnetic inversion. *Geology* 40(3):215–218.

595 Gamble, T. D., Goubau, W. M., Clarke, J., 1979. Magnetotellurics with a remote magnetic
596 reference. *Geophysics* 44(1), 53-68.

597 Gessner, K., Gallardo, L.A., Wedin, F., Sener, K., 2016. Crustal structure of the northern
598 Menderes Massif, western Turkey, imaged by joint gravity and magnetic inversion. *Int. J.*
599 *Earth Sci. (Geol Rundsch)*, 105: 2133.

600 Glover, P. W. J., 1996. Graphite and Electrical Conductivity in the Lower Continental Crust: A
601 Review. *Phys. Chem. Earth*. 21 (4), 279-287.

602 Heise, W., T. G. Caldwell, H. M. Bibby, Brown, C. 2006. Anisotropy and phase splits in
603 magnetotellurics. *Physics of the Earth and Planetary Interiors* 158, 107–121.

604 Hirdes, W., Davis, D. W., Lüdtke, G., Konan, G., 1996. Two generations of Birimian
605 (Paleoproterozoic) volcanic belts in northeastern Côte d'Ivoire (West Africa): consequences for
606 the "Birimian controversy". *Precambrian Research* 80, 173-191.

607 Hyndman, R. D., Vanyan, L. L., Marquis, G., Lawa, L. K., 1993. The origin of electrically
608 conductive lower continental crust: saline water or graphite? *Physics of the Earth and Planetary*
609 *Interiors* 81(1-4), 325-345.

610 Jessell, M., Begg, G.C., Miller, M.S., 2016. The geophysical signatures of the West African
611 Craton. *Precambrian Research*, 274, 3-24.

612 Jones, A.G., 1987. MT and reflection: an essential combination. *Geophysical Journal of the*
613 *Royal Astronomical Society*, 89, 7-18.

614 Jones, A. G., 1992. *The Continental Lower Crust*, D. M. Fountain, R. J. Arculus and R. W. Kay
615 Edition. Elsevier, New York, Ch. Electrical conductivity of the continental lower crust, pp. 81-
616 143.

617 Jones, A.G., Kurtz, R.D., Boerner, D.E., Craven, J.A., McNeice, G.W., Gough, D.I., Delaurier,
618 J.M., Ellis, R.G., 1992. Electromagnetic constraints on strike-slip-fault geometry - the Fraser
619 River fault system. *Geology*, 20, 561-564.

620 Jones, A. G., Jödicke, H., 1984. Magnetotelluric transfer function estimation improvement by a
621 coherence-based rejection technique. 54th Ann. Mtg. Soc. of Expl. Geophys., Atlanta, Georgia.

622 Khoza, D., Jones, A. G., Muller, M. R., Evans, R. L., Webb, S. J., Miensopust, M., the SAMTEX
623 team, 2013. Tectonic model of the Limpopo belt: Constraints from magnetotelluric data.
624 Precambrian Research, 226.

625 Kiyan, D., Jones, A.G., Vozar, J., 2013. The inability of magnetotelluric off-diagonal impedance
626 tensor elements to sense oblique conductors in three-dimensional inversion. Geophys. J. Int. 196,
627 1351–1364.

628 Kříbek, B., Sýkorová, I., Machovič, V., Laufek, F., 2008. Graphitization of organic matter and
629 fluid-deposited graphite in Palaeoproterozoic (Birimian) black shales of the Kaya-Goren
630 greenstone belt (Burkina Faso, West Africa). Journal of Metamorphic Geology 26, 937-958.

631 Ledo, J., 2005. 2-D versus 3-D magnetotelluric data interpretation. Surveys in Geophysics 26,
632 511-543.

633 Lemoine, S., 1990. Le faisceau d'accidents Greenville-Ferkessedougou-Bobo-Dioulasso
634 (Libéria, Côte d'Ivoire, Burkina Faso); témoin d'une collision oblique éburnéenne. 15e colloque
635 de géologie africaine. CIFEG, Paris, Nancy, France, 67-70.

636 Leube, A., Hirdes, W., Mauer, R., Kesse, G. O., 1990. The early Proterozoic Birimian
637 Supergroup of Ghana and some aspects of its associated gold mineralization. Precambrian
638 Research 46, 139-165.

639 Loh, G., Hirdes, W., 1996. Explanatory notes for the geological map of south-west Ghana 1:100
640 000-Sheets Sekondi (0402a) and Axim (0403b). Ghana Geol. Surv. Bull. 49 (63).

641 Lompo, M., 2010. Paleoproterozoic structural evolution of the Man-Leo Shield (West Africa)
642 Key structures for vertical to transcurrent tectonics. *Journal of African Earth Sciences* 58 (19-
643 36).

644 Lüdtké, G., Hirdes, W., Konan, G., Koné, Y., N'da, D., Traoré, Y., Zamblé, Z., 1999. Géologie
645 de la région Haute Comoé Sudfeuilles Dabakala (2b, d et 4b, d). Direction de la Géologie
646 Abidjan Bulletin 176.

647 Mareschal, M., 1986. Modeling of natural source of magnetospheric origin in the interpretation
648 of regional induction studies: a review. *Surveys in Geophysics* 8, 261–300.

649 Metelka, V., Baratoux, L., Naba, S., Jessell, M. W., 2011. A geophysically constrained litho-
650 structural analysis of the Eburnean greenstone belts and associated granitoid domains, western
651 Burkina Faso. *Precambrian Research* 190, 48-69.

652 Miensopust, M., Jones, A. G., Muller, M. R., Garcia, X., Evans, R. L., 2011. Lithospheric
653 structures and Precambrian terrane boundaries in northeast-ern Botswana revealed through
654 magnetotelluric profiling as part of the Southern African Magnetotelluric Experiment. *Journal of*
655 *Geophysical Research - Solid Earth* 116 (B02401).

656 Muller, M. R., Jones, A. G., Evans, R. L., Grütter, H. S., Hatton, C., Garcia, X., Hamilton, M. P.,
657 Miensopust, M. P., Cole, P., Ngwisanyi, T., Hutchins, D., Fourie, C. J., Jelsma, H. A., Evans, S.
658 F., Aravanis, T., Pettit, W., Webb, S. J., Wasborg, J., The SAMTEX Team, 2009. Lithospheric
659 structure, evolution and diamond prospectivity of the Rehoboth Terrane and western Kaapvaal
660 Craton, southern Africa: Constraints from broadband magnetotellurics. *Lithos.* 112S, 93-105.

661 Pasyanos, M. E., Nyblade, A. A., 2007. A top to bottom lithospheric study of Africa and Arabia.
662 Tectonophysics 444, 27-44.

663 Pons, J., Barbey, P., Dupuis, D., Leger, J. M., 1995. Mechanisms of pluton emplacement and
664 structural evolution of a 2.1 Ga juvenile continental crust: the Birimian of southwestern Niger.
665 Precambrian Research, 281-301.

666 Ritz, M., 1983. Use of the Magnetotelluric method for a better Understanding of the West
667 Africa Shield. Journal of Geophysical Research 88 (B12), 10,625-10,633.

668 Ritz, M., 1984. Inhomogeneous Structure of the Senegal Lithosphere From Deep
669 Magnetotelluric Soundings. Journal of Geophysical Research 89 (B13), 11,317-11,331.

670 Rodi, W., Mackie, R. L., 2001. Nonlinear conjugate gradients algorithm for 2D magnetotelluric
671 inversion. Geophysics 66, 174-187.

672 Rooney, A.D., Selby, D., Houzay, J.-P., Renne, P.R. 2010. Re–Os geochronology of a
673 Mesoproterozoic sedimentary succession, Taoudeni basin, Mauritania: Implications for basin
674 wide correlations and Re–Os organic-rich sediments systematic. Earth and Planetary Science
675 Letters, 289, no. 3-4, pp. 486-496.

676 Rousseeuw, P.J., 1984. Least median of squares regression, Journal of the American Statistical
677 Association, 79, 871-880.

678 Selway, K., Hand, M., Heinson, G. S., Payne, J. L., 2009. Magnetotelluric constraints on
679 subduction polarity: Reversing reconstruction models for Proterozoic Australia. Geology 37 (9),
680 799-802.

681 Sheriff, R.E., 1984, Encyclopedic dictionary of exploration geophysics (2nd ed.): Tulsa, OK,
682 Society of Exploration Geophysicists, p. 323.

683 Siripunvaraporn, W., Egbert, G., Lenbury, Y., Uyeshima, M., 2005. Three-dimensional
684 magnetotelluric inversion: data-space method. *Physics of the Planetary Interiors* 150, 3-14.

685 Smirnov, M.Y., 2003. Magnetotelluric data processing with a robust statistical procedure having
686 a high breakdown point. *Geophys. J. Int.* 152, 1–7.

687 Spratt, J. E., Jones, A. G., Jackson, V. A., Collins, L., Avdeeva, A., 2009. Lithospheric geometry
688 of the Wopmay orogen from a Slave craton to Bear Province magnetotelluric transect. *Journal of*
689 *Geophysical Research* 114 (B01101).

690 Schwartz, M.O., Melcher, F., 2003. The Perkoa zinc deposit, Burkina Faso. *Economic Geology*
691 98, 1463–1485.

692 Teal, D.J., Kah, L.C., 2005. Using C-isotopes to constrain interbasinal stratigraphic correlations,
693 Mesoproterozoic Atar Group, Mauritania. *Geological Society of America, Abstracts with*
694 *Programs* 37, 45.

695 Vidal, M., Gumiaux, C., Cagnard, F., Pouclet, A., Ouattara, G., Pichon, M., 2009. Evolution of a
696 paleoproterozoic "weak type" orogeny in the West African Craton (Ivory Coast). *Tectonophysics*
697 477, 145159.

698 Wannamaker, P. E., 2000. Comment on "the petrologic case for a dry lower crust" by Bruce W.
699 D. Yardley and John W. Valley. *Journal of Geophysical Research* 105 (B3), 6057-6064.

700 Wei, W., F. L. Pape, A. G. Jones, J. Vozar, H. Dong, M. J. Unsworth, S. Jin, G. Ye, J. Jing, L.
701 Zhang, Xie, C., 2014. Northward channel flow in northern Tibet revealed from 3D
702 magnetotelluric modelling. *Physics of the Earth and Planetary Interiors*, 235, 13–24.

703 Yardley, W. D., Valley, W., 1997. The petrologic case for a dry lower crust. *J. Geophys. Res.*
704 102, 12,173-12,185.

705 Yoshino, T. and Noritake, F., 2011. Unstable graphite films on grain boundaries in crustal rocks,
706 *Earth and Planetary Science Letters*, 306, 186-192.

707

708

709

710

711

712

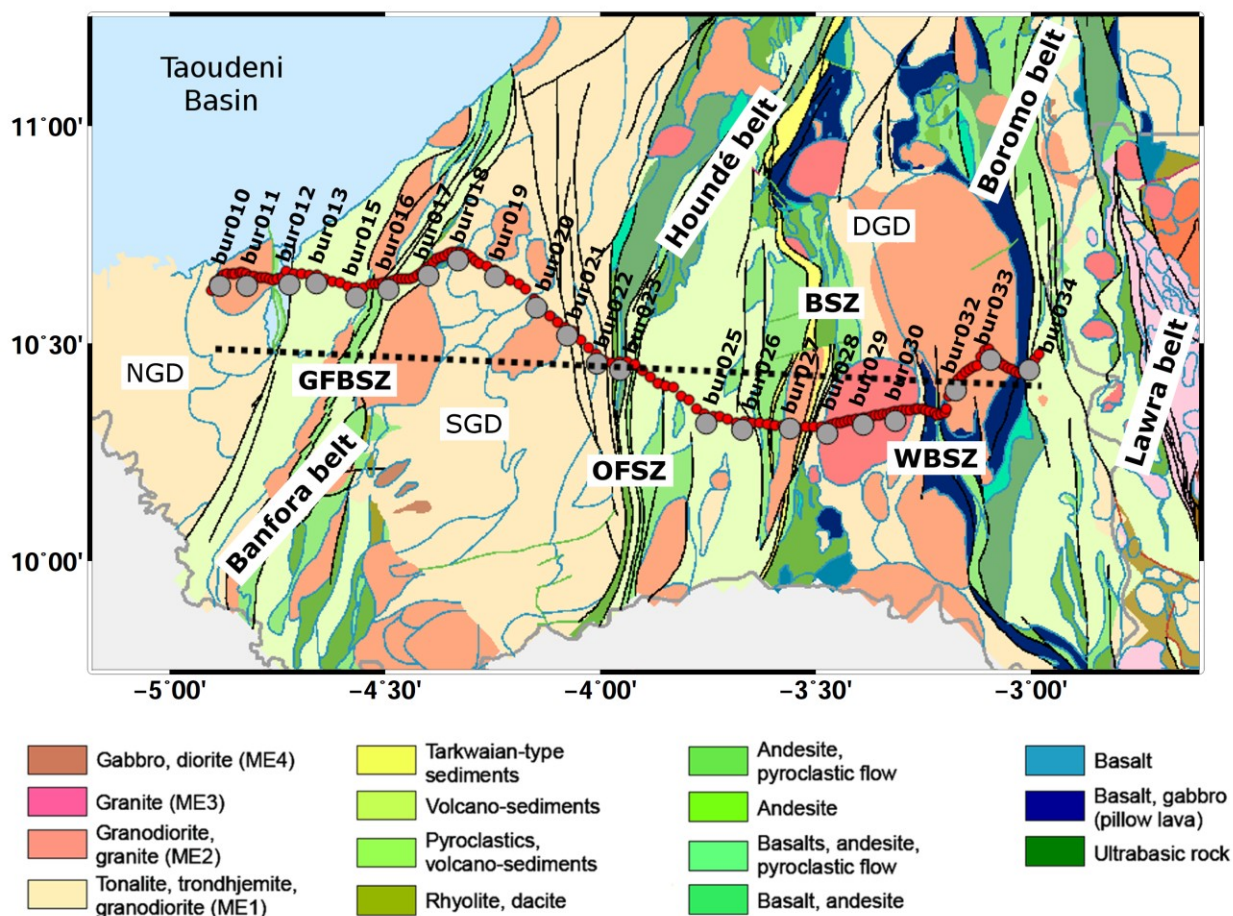
713

714

715

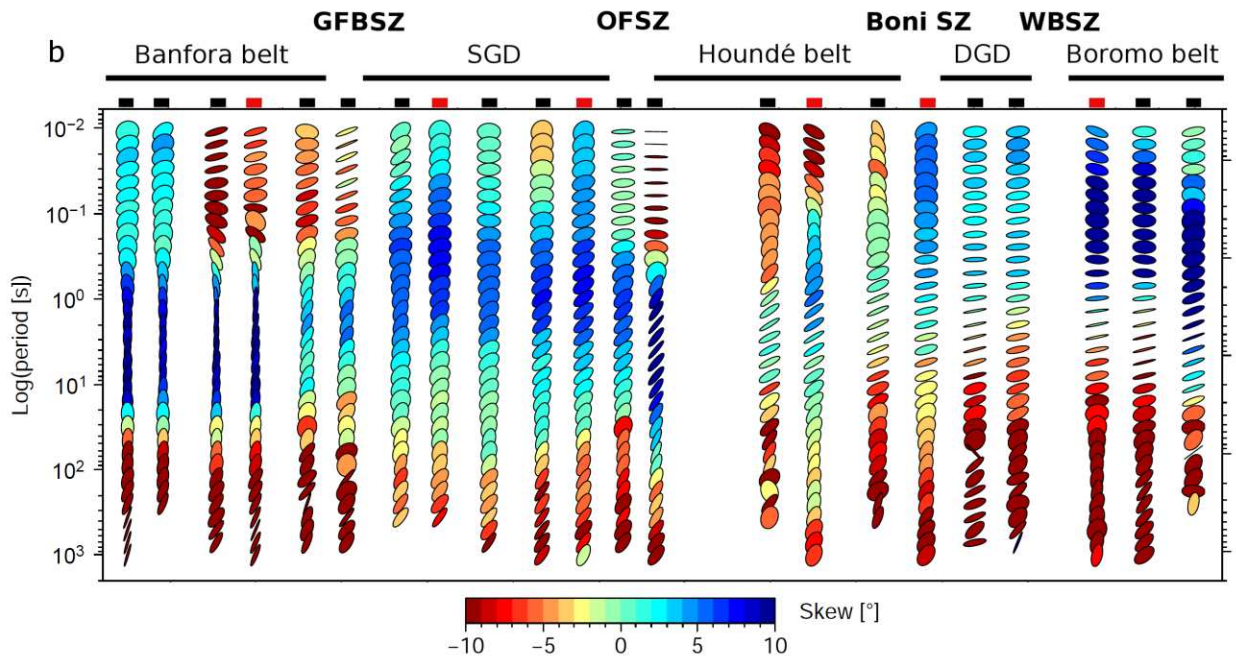
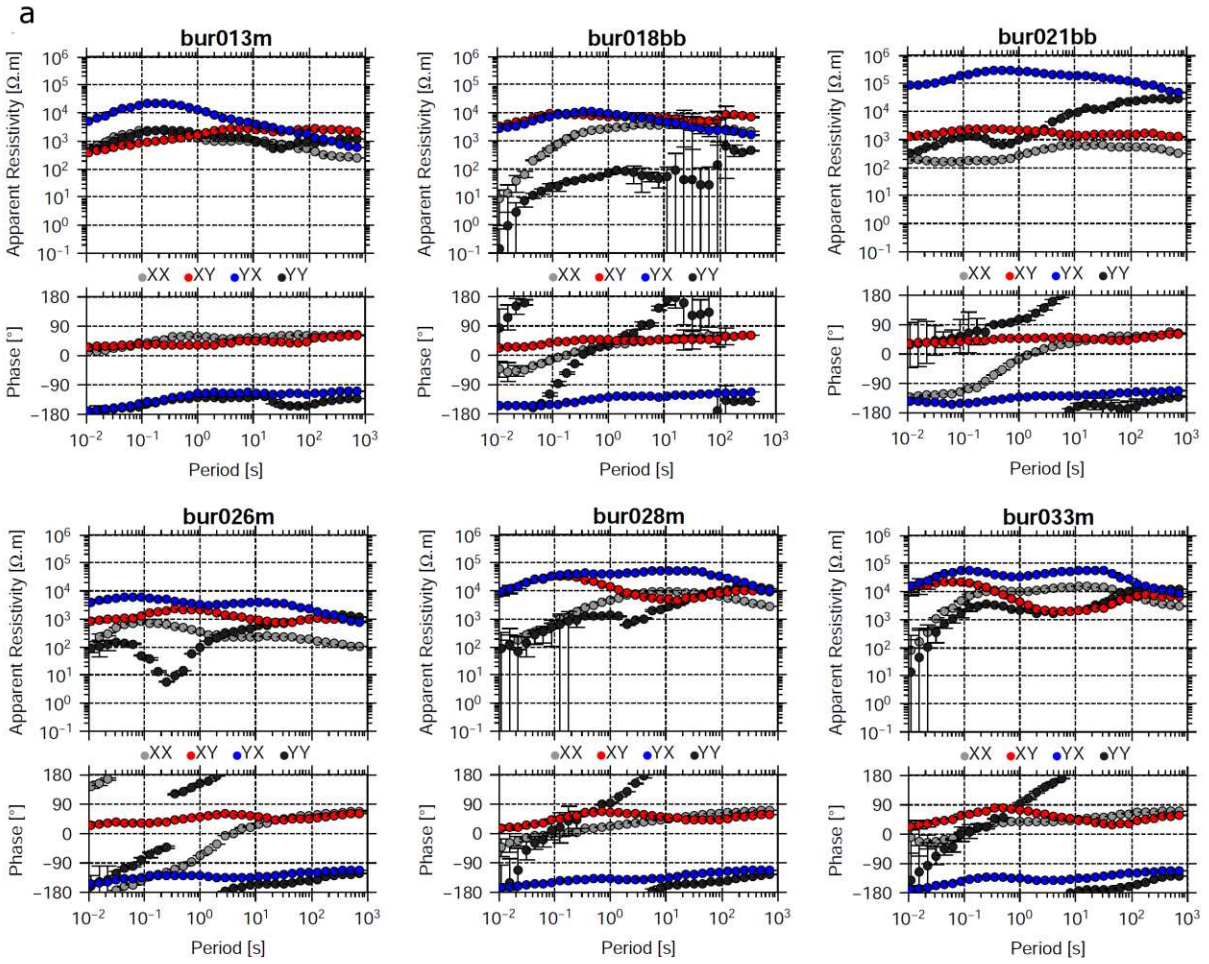
716

717

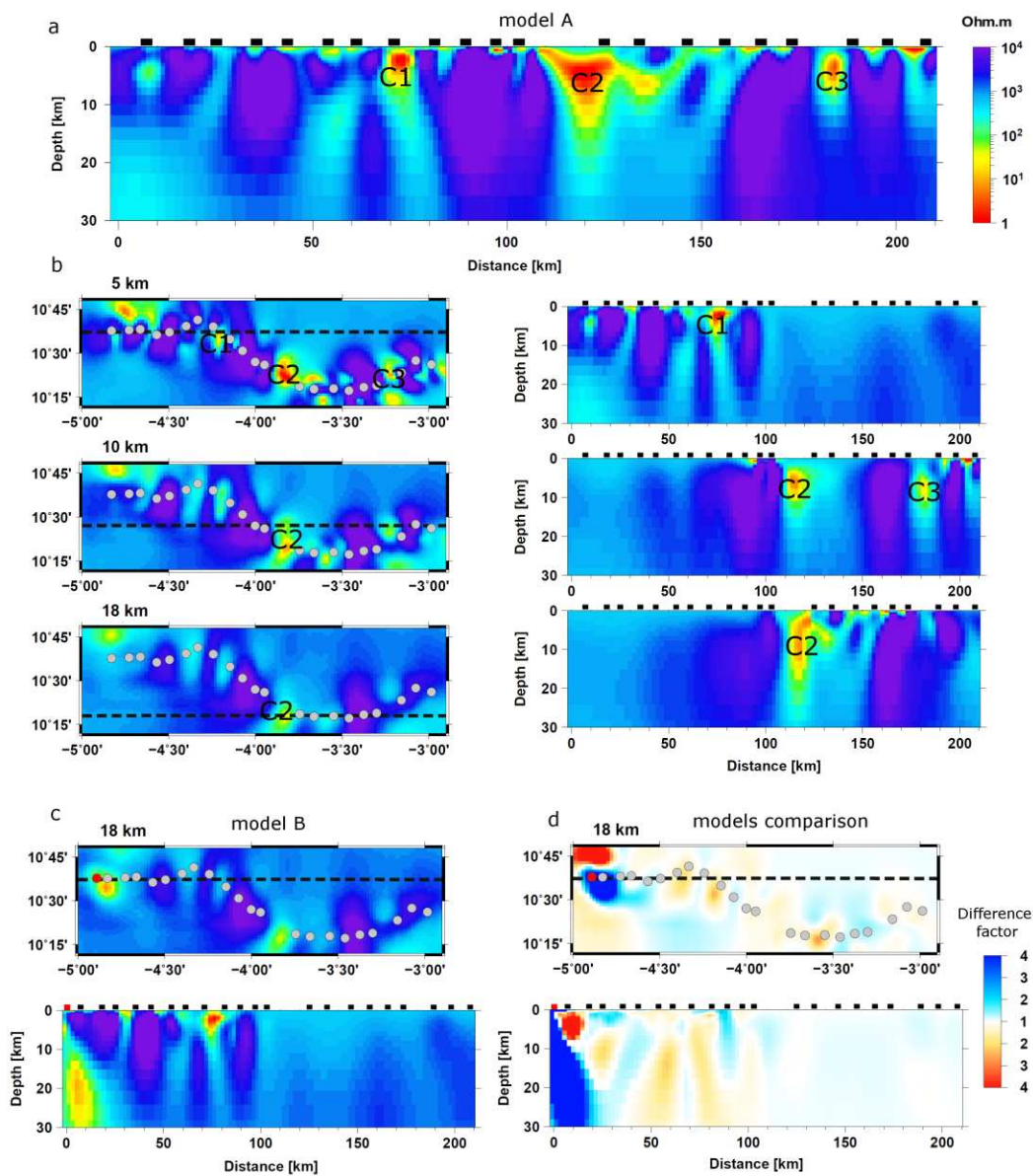


719

720 Figure 1: Geological map of the study area (modified from Baratoux et al., 2011; Metelka et al.,
 721 2011; Block et al., 2015) showing major structural and geological features. The locations of the
 722 MT sites are represented as dark grey dots. The red dots represent the ground gravity
 723 measurement points. The black dotted line defines the location of the 2D density/magnetization
 724 geospectral image issued from joint inversion of gravity and aeromagnetic data. NGD =
 725 Niangoloko Granitoid Domain; GFBSZ = Greenville-Ferkessedougou-Bobo Dioulasso Shear
 726 Zone; SGD = Sidéradougou Granitoid Domain; OFSZ = Ouango-Fitini Shear Zone; BSZ = Boni
 727 Shear Zone; DGD = Diébougou Granitoid Domain; WBSZ = West Batié Shear Zone.

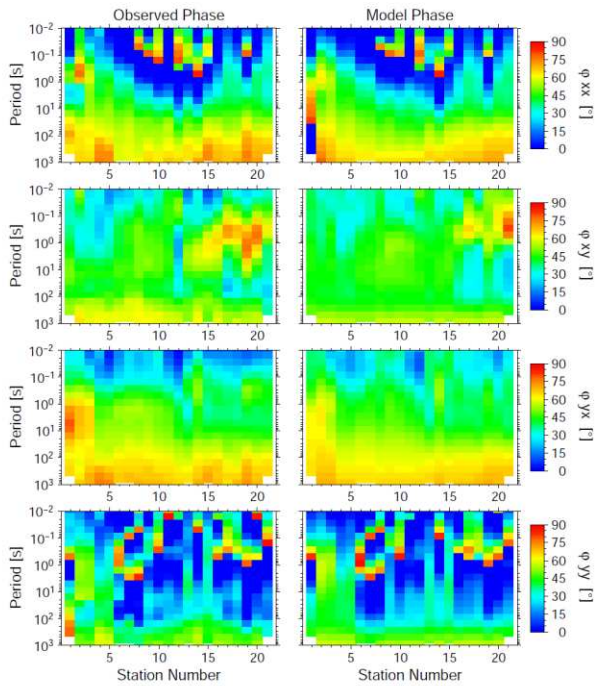
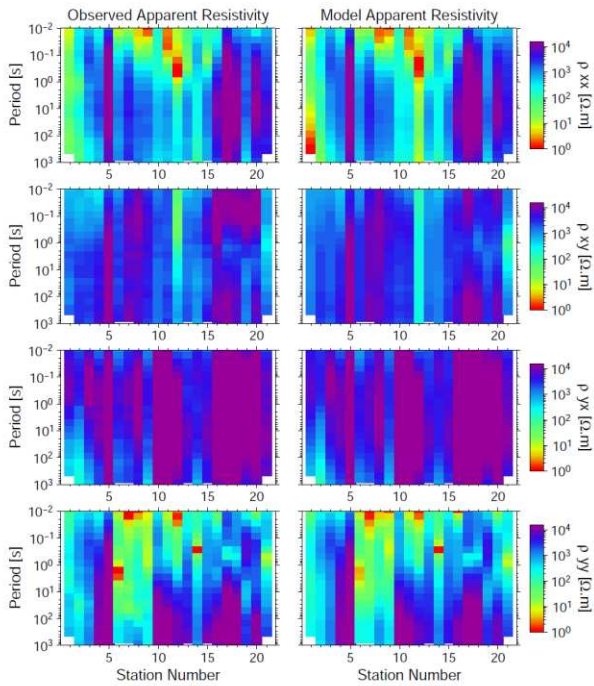
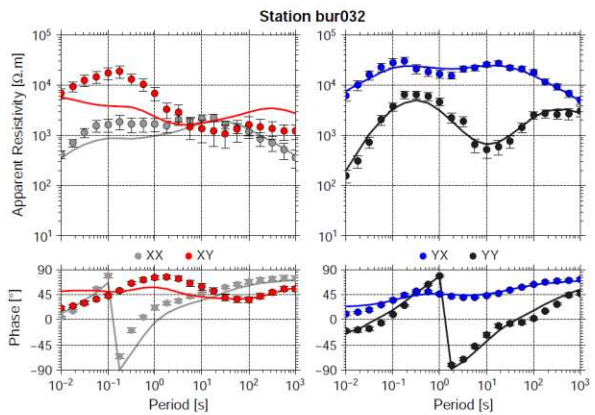
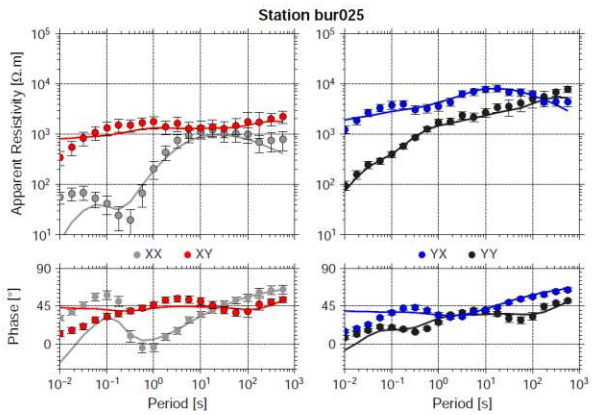
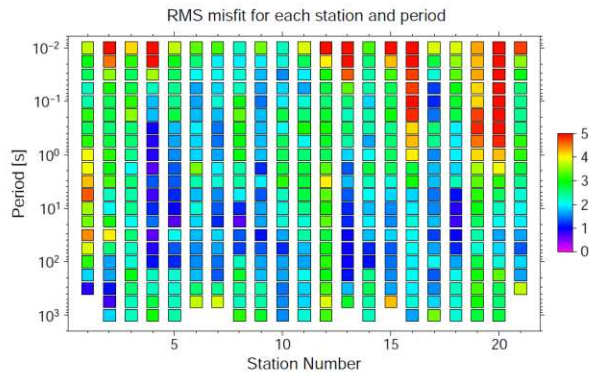
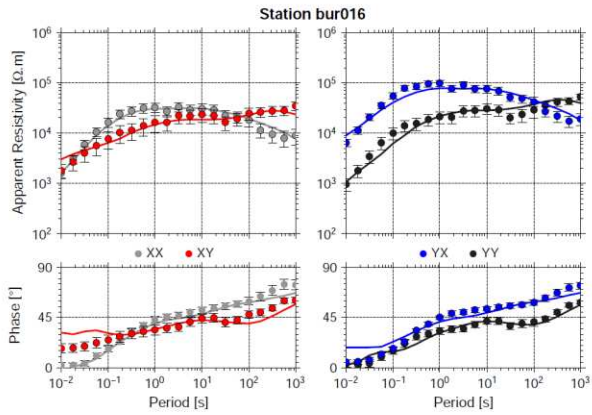


729 Figure 2: a - MT full responses in apparent resistivity and phase for selected broadband (bb) and
 730 merged (m) sites along the profile. b - Phase tensor ellipses for all periods of each MT sites. The
 731 ellipses are normalized by their major axis and filled with the skew angle. The phase tensor
 732 ellipses are plotted so that the horizontal orientation corresponds to an east–west orientation.
 733



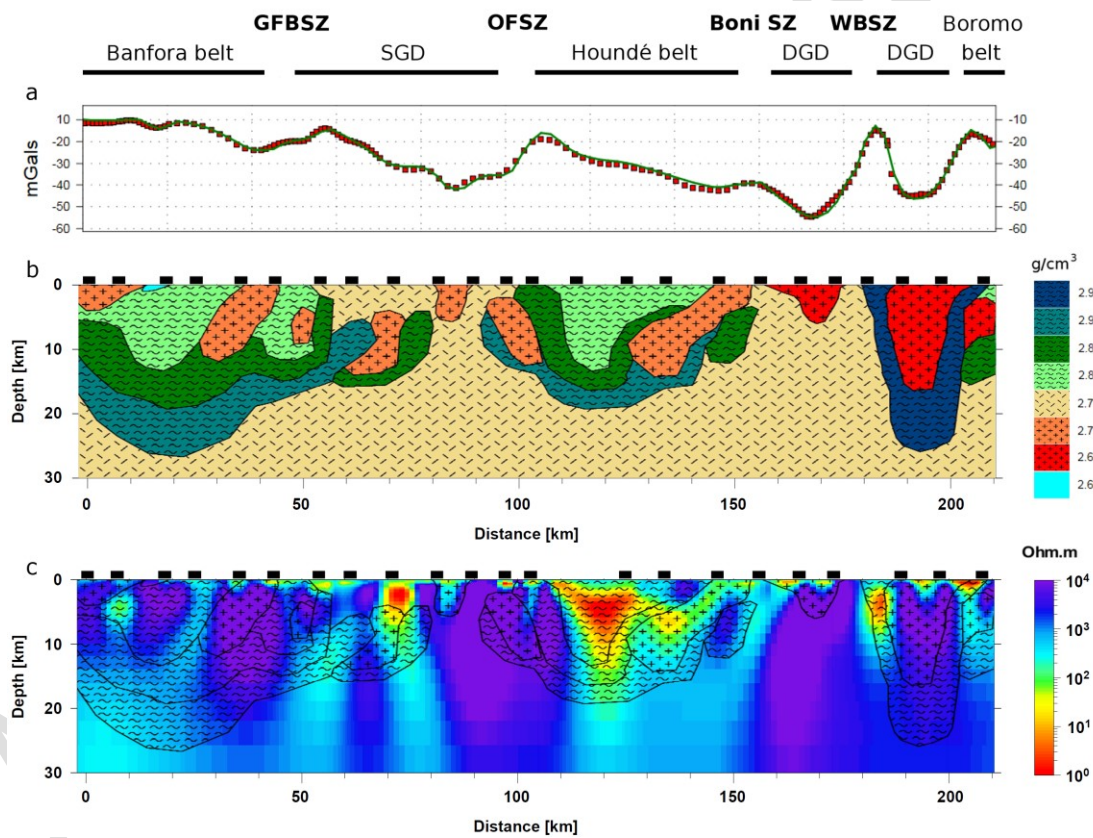
735 Figure 3: a – 2D cross-section representative of 3D model A; b – 3D model A: Horizontal slices
736 for different depths as well as vertical cross-sections (locations defined by black dashed lines); c
737 – 3D model B: 18 km depth horizontal and a vertical cross-section (location defined by black
738 dashed line) highlighting the presence of the lower crustal conductor below station bur010; d –
739 Comparison of the resistivity ratio between model A and B: blue meaning A is more conductive
740 than B and red meaning B is more conductive than A.

Accepted Manuscript



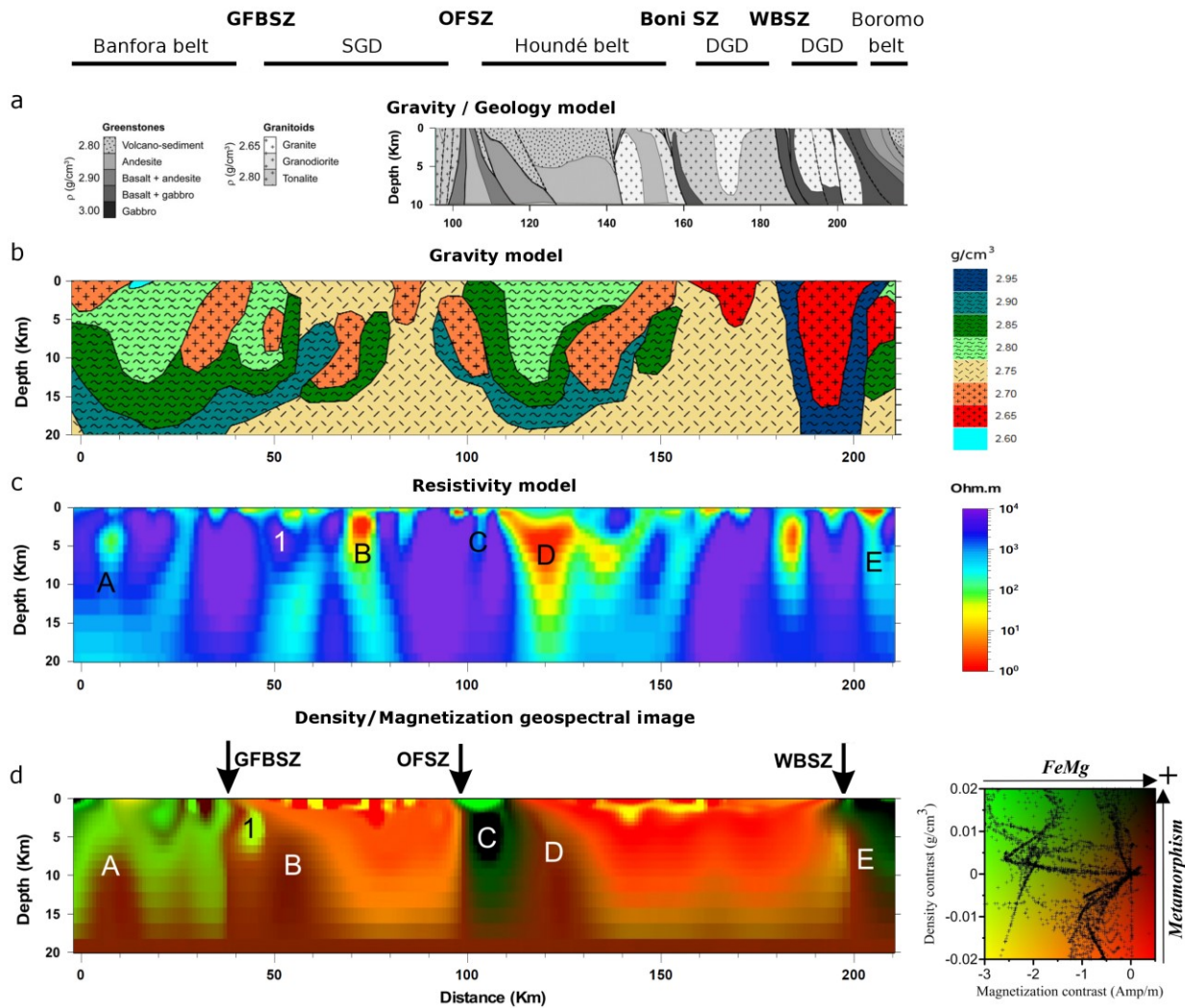
742 Figure 4: Observed and predicted apparent resistivity and phase responses for 3D model A. The
 743 fit between the observed (dots) and modelled (lines) 4 components curves for 3 particular sites is
 744 shown as well as the normalized misfit between observed and calculated data for each station
 745 and each period. At the bottom, all responses are plotted for all 4 components of the impedance
 746 tensor as a function of period and station location along the MT profile. Station numbers are
 747 increasing from west to east.

748



749

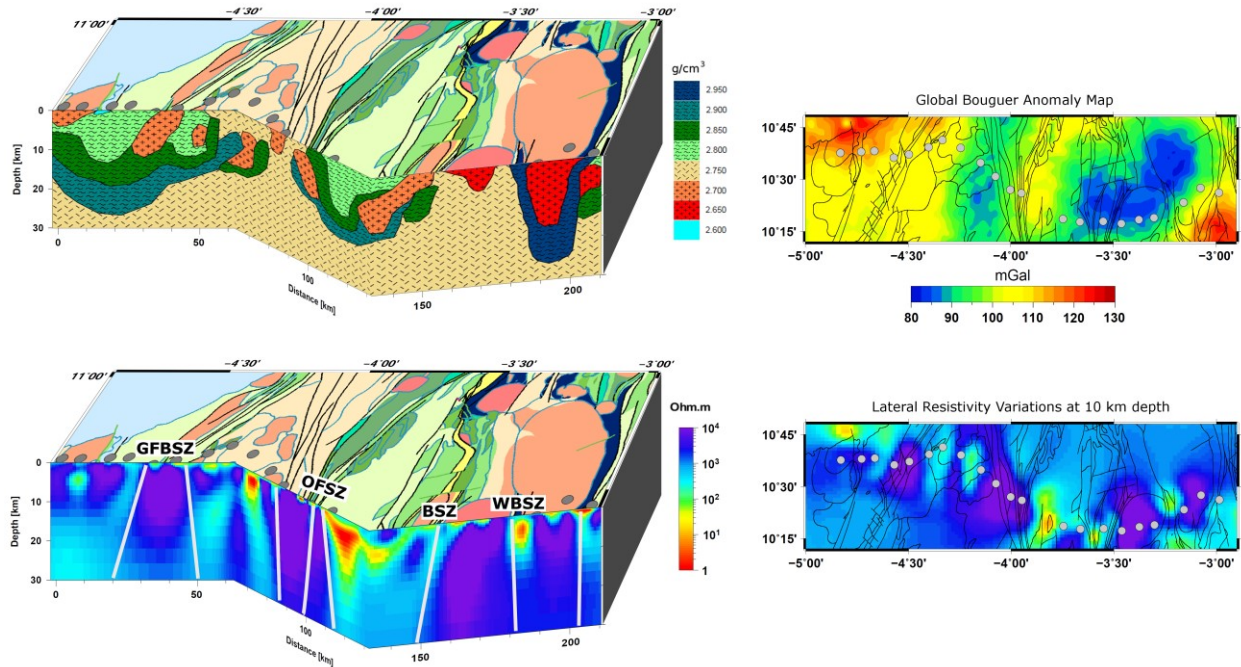
750 Figure 5: a – Gravity Bouguer anomaly; b – Density model derived from forward modeling of
 751 the ground gravity data; c - Comparison of the gravity model with the resistivity structures
 752 obtained from MT modeling.



754

755 Figure 6: Comparison of different geophysical models for the crust of southern Burkina Faso. a -
 756 Gravity/geology forward model from Baratoux et al. (2011); b - Preferred density model derived
 757 from forward modeling of ground gravity data; c - Resistivity model derived from MT 2D
 758 inversion; d - Density and magnetic geospectral representation issued from the joint inversion of
 759 gravity and magnetic data. The associated colors represent the relationship between density and
 760 magnetization contrasts.

761



762

763 Figure 7: Correlation between the density and resistivity contrasts of the crust at depth with
 764 surficial lithologies of southern Burkina Faso. The crustal scale resistivity contrasts interpreted
 765 as involved with major shear zones are highlighted in light grey. GFBSZ = Greenville-
 766 Ferkessedougou-Bobo Dioulasso Shear Zone; OFSZ = Ouango-Fitini Shear Zone; BSZ = Boni
 767 Shear Zone; WBSZ = West Batié Shear Zone. Lateral variations of the electrical resistivity at 10
 768 km are also compared with the Bouguer anomaly map derived from the global 2 min resolution
 769 WGM2012 model (Balmino et al., 2012).

770

771